ARTICLE IN PRESS

Communications Physics

https://doi.org/10.1038/s42005-026-02517-7

Article in Press

Observation and extended Weiss modeling of multi-step type-II spin switching in Mn doped $YbFeO_3$

Received: 6 August 2025

Accepted: 15 January 2026

[redacted]

Cite this article as: Yang, W., Peng, H., Guo, Y. *et al.* Observation and extended Weiss modeling of multi-step type-II spin switching in Mn doped $YbFeO_3$. *Commun Phys* (2026). https://doi.org/10.1038/s42005-026-02517-7

Wanting Yang, Haohuan Peng, Yefei Guo, Xiaoxuan Ma, Baojuan Kang, Rongrong Jia, Jun-Yi Ge, Yuriy Dedkov & Shixun Cao

We are providing an unedited version of this manuscript to give early access to its findings. Before final publication, the manuscript will undergo further editing. Please note there may be errors present which affect the content, and all legal disclaimers apply.

If this paper is publishing under a Transparent Peer Review model then Peer Review reports will publish with the final article.

ARTICLE IN PRESS

© The Author(s) 2026. **Open Access** This article is licensed under a Creative Commons Attribution-NonCommercial-NoDerivatives 4.0 International License, which permits any non-commercial use, sharing, distribution and reproduction in any medium or format, as long as you give appropriate credit to the original author(s) and the source, provide a link to the Creative Commons licence, and indicate if you modified the licensed material. You do not have permission under this licence to share adapted material derived from this article or parts of it. The images or other third party material in this article are included in the article's Creative Commons licence, unless indicated otherwise in a credit line to the material. If material is not included in the article's Creative Commons licence and your intended use is not permitted by statutory regulation or exceeds the permitted use, you will need to obtain permission directly from the copyright holder. To view a copy of this licence, visit http://creativecommons.org/licenses/by-nc-nd/4.0/.

Observation and extended Weiss modelling of multi-step type-II spin switching in Mn doped $YbFeO_3$

Wanting Yang[1,2], Haohuan Peng[1], Yefei Guo[3], Xiaoxuan Ma[1,4], Baojuan Kang[1], Rongrong Jia[1],
Jun-Yi Ge[1], Yuriy Dedkov[5], Shixun Cao[1*]

[1]*Materials Genome Institute, Institute of Quantum Science and Technology, International Center for Quantum and Molecular Structures, Shanghai University, Shanghai, 200444, China*

[2]*Institute of Physics, Johannes Gutenberg University Mainz, Mainz, 55128, Germany*

[3]*School of Physics and Advanced Energy, Henan University of Technology, Zhengzhou, Henan, 450001, China*

[4]*School of Material Science and Engineering, Shanghai University, Shanghai 200444, China*

[5]*Institute of Physics, Centre for Advanced Laser Techniques, Zagreb, 10000, Croatia*

[*]Email: sxcao@shu.edu.cn

Controlling magnetic states with minimal energy input promises faster and more efficient devices. However, achieving programmable, multi-level spin switching in antiferromagnetic materials remains a challenge. Here we observe both conventional and multi-step type-II spin switching, as well as its coupling with spin reorientation transition, in a 5% manganese-doped single crystal of ytterbium orthoferrite. The stability of ytterbium ions magnetic moments, ensured by its nearly filled 4*f* shell, combined with reduced molecular field strength due to manganese substitution, enables controlled reversal of the rare-earth spins. To interpret these observations, we extend the classical Weiss model by introducing distributed effective fields acting on magnetically inequivalent rare-earth components. This generalized framework accounts quantitatively for the multi-step spin switching behavior. Our results demonstrate a pathway to engineer complex spin transitions via internal field modulation, and offer insights into rare-earth-driven spin-state control, potentially useful for polymorphic spin memory and programmable antiferromagnetic switching.

Introduction

Antiferromagnetic materials have attracted wide attention for spintronic and memory applications due to their intrinsic magnetic stability, lack of stray fields, and ultrafast spin dynamics[1–3]. Among them, rare-earth orthoferrites (RFeO$_3$, RFOs) offer a particularly rich platform for exploring spin dynamics and spin transport, owing to the strong interactions between the rare-earth (R^{3+}) and Fe^{3+} magnetic sublattices[4–7]. One key manifestation of this interplay is spin switching (SSW), wherein the net magnetic moment of one or both sublattices reverses under thermal or magnetic perturbations [4,8–10]. In particular, type-II SSW, where only the spin of R^{3+} flips, offers an appealing route for low-field spin manipulation[11]. In RFO compounds, this process typically occurs above the Néel temperature of R^{3+} sublattice, and the spin reversal therefore arises from the response of the R^{3+} moments to the molecular field generated by the ordered Fe^{3+} sublattice. Recently, multi-step SSWs have also been reported, in which the R^{3+} moments switch in discrete stages, suggesting the potential for multi-level spin-state control within a single-phase crystal[12,13].

Despite these intriguing possibilities, type-II and multi-step SSWs remain rarely observed in transition-metal-doped RFOs. This is largely attributed to the perturbation of delicate R-Fe exchange interactions by 3*d* dopants, which can disrupt the superexchange pathways essential for coherent spin flipping. Previous studies for SSW have primarily focused on R-site substitution, which introduces additional R-R and R-Fe couplings, complicating the energy landscape and obscuring the intrinsic mechanism of SSW[14–16]. Fe-site doping, on the other hand, offers a potentially cleaner means to modulate the Fe^{3+} molecular field while preserving sublattice symmetry. However, prior studies have shown that even low-level transition-metal substitution can suppress SSW entirely, likely due to the disruption of Fe-O-Fe superexchange interactions and orbital incompatibility[17,18]. For example, Cr^{3+}, Co^{3+}, or Ni^{3+} doping tends to suppress the weak ferromagnetism, introduce spin dilution or low-spin configurations, which suppresses the SSW behavior[19–21].

Here, we investigate 5% Mn-doped YbFeO$_3$ (YFMO) as a model system to probe the feasibility of SSW in Fe-site doped crystal. The magnetically stable R sublattice provided by Yb^{3+}, with its nearly filled 4*f* shell, enables clear identification of R-driven transitions. Mn^{3+} as the Fe-site dopant is particularly motivated by its $3d^4$ electronic configuration, which is similar to Fe^{3+} ($3d^5$) yet introduces active orbital degrees of freedom and moderate Jahn-Teller distortion. Such substitution maintains the orthorhombic *Pbnm* symmetry while slightly adjusting the Fe-O-Fe bond geometry and internal molecular field. In this system, we observe both conventional and multi-step type-II SSWs, along with their coupling to the spin reorientation transition (SRT). To describe these behaviors, we extend the classical Weiss model by introducing effective fields acting on different R^{3+}. This framework reproduces the experimentally observed stepwise transitions and provides a more general mechanism for type-II SSW. These findings highlight the potential of internal field modulation via Fe-site substitution as a strategy for controlling spin states in orthoferrites, with implications for multi-state magnetic memory and programmable antiferromagnetic switching.

Results and discussion

Structural characterization

Fig. 1a shows the Rietveld refinement of the powder X-ray diffraction pattern of YFMO, conducted using the FullProf Suite with a Pseudo-Voigt profile (the peaks between 32.5° and 39° are showed in the Supplementary Figure 1)[22]. The data are well described by the orthorhombic perovskite structure (space group *Pbnm*), yielding good agreement with experimental data, with refinement indicators $R_{\mathrm{wp}} = 9.4$ and $\chi^2 = 1.2$. No impurity phases or preferred orientation effects are detected. The refined lattice parameters are $a = 5.2314$ (5) Å, $b = 5.5570$ (2) Å, and $c = 7.5700$ (6) Å. For, undoped $YbFeO_3$, $a = 5.2327(2)$ Å, $b = 5.5654(9)$ Å, and $c = 7.5718(2)$ Å[23]. The lattice parameters a and c slightly decrease whereas b increases, following the same trend observed in other Mn-doped *R*FOs[24,25].

Quantitative X-ray photoelectron spectroscopy (XPS) was used to examine the chemical valence states after ultra-high vacuum annealing. High-resolution spectra (Fig. 1b) show Fe^{3+} peaks at 711.3 eV ($2p_{3/2}$) and 724.6 eV ($2p_{1/2}$), and Mn^{3+} peaks at 641.6 eV ($2p_{3/2}$) and 653.3 eV ($2p_{1/2}$), respectively. A weak shoulder near the Mn $2p_{3/2}$ peak suggests a minor Mn^{2+} contribution, likely induced by surface reduction during annealing. The overall valence states remain trivalent-dominated. Quantitative XPS analysis (Fig. 1c) confirms the stoichiometry, yielding a Yb: Fe: Mn: O atomic ratio of 0.996: 0.947: 0.052: 3.00. The homogeneous distribution of Mn shown in Supplementary Figure 2 confirms that the nominal composition (5% Mn substitution at Fe sites) is well maintained throughout the crystal. The supplementary data for this study are publicly available[26].

The crystal and magnetic structure are visualized in Fig. 1d based on Rietveld-refined data using VESTA[27]. YFMO adopts an orthorhombically distorted perovskite framework with corner-sharing Fe/MnO_6 octahedra. The Fe-O-Fe bond angle 140.1214 (2)° deviates from 180°, leading to octahedral tilting. Comparing the undoped value of 142.8383 (0)°, the decrease in bond angle reflects the structural distortion induced by Mn substitution. The distortion percentage calculated by $(180^\circ - \theta_{\text{Fe-O-Fe}}) / 180^\circ \times 100\%$ increases from 20.9% ($YbFeO_3$) to 22.2% (YFMO). This distortion weakens the Fe-O-Fe superexchange interaction, which is proportional to $\cos^2\theta$ and enhances the antisymmetric Dzyaloshinskii-Moriya interaction (DMI) because of the inversion symmetry breaking enhancement, thereby influencing magnetic coupling[28]. The magnetic ground state at room temperature corresponds to the canted antiferromagnetic Γ_4 (G_x, F_z) configuration, with the Néel vector $\boldsymbol{n}$ oriented along the *a*-axis and a weak ferromagnetic moment of Fe^{3+} sublattice $\delta\mathbf{m}_{\text{Fe}}$ along *c*-axis, as illustrated in Fig. 1e. Laue back-reflection (Fig. 1f) and high-resolution X-ray diffraction (XRD) along the *c*-axis (Fig. 1g) further confirm the high crystalline quality and proper orientation, as evidenced by sharp symmetric Laue spots and (00*l*) reflections without detectable impurity peaks.

Magnetic characterization

Fig. 2 shows the temperature-dependent magnetization (*M*-*T*) curves under various magnetic fields applied along the *c*-axis. Type-II SSWs are observed between 20 and 120 Oe, with clear field-dependent tunability. The associated spin-flip configurations are illustrated by the blue and orange arrows. While Yb^{3+} remains paramagnetic at the SSW temperature, it carries an induced net magnetic moment arising from the Fe^{3+} molecular field ($\delta\mathbf{m}_{\text{Yb}}$). $\delta\mathbf{m}_{\text{Yb}}$ flipping gives rise to the SSW. Compared with undoped $YbFeO_3$, the critical field required to induce SSW in YFMO is significantly reduced, suggesting that Mn doping lowers the threshold for R^{3+} spin reversal[23,29]. The switching temperature is tunable over a wide range, from 200 K down to 9 K, by adjusting the external field within a low-field window. This enhanced sensitivity enables access to both single-step and multi-step switching regimes, as illustrated in Fig. 2b-e. At fields below 30 Oe, partial spin flipping of Yb^{3+} moments occurs due to the competition between the external field and the internal molecular field originating from the Fe^{3+} sublattice. Upon cooling, the accumulated internal field energy surpasses the threshold for further spin flipping, leading to a multi-step SSW. At higher fields, the increased Zeeman energy favors collective flipping of $\delta\mathbf{m}_{\text{Yb}}$, which aligns antiparallel to $\delta\mathbf{m}_{\text{Fe}}$, producing a typical type-II SSW. Furthermore, in the intermediate range of 50-90 Oe, the coupling between the two sublattices becomes disrupted, and multi-step SSW reappears. With magnetic fields above 100 Oe, only conventional SSWs appear in *M*-*T* curves. The observed SSW behaviors are enabled by the dual role of Mn doping: it weakens the Fe^{3+} sublattice molecular field, thus reducing the *R*-Fe coupling; and simultaneously, preserves rare-earth magnetic activity due to the nearly filled 4*f* shell of Yb^{3+}. At fields above 120 Oe, the switching becomes fully suppressed, indicating that the effective internal field becomes too strong for thermally driven spin reversal to occur. These findings emphasize the effectiveness of internal field engineering in controlling complex spin transitions without the need for large external fields, highlighting a promising strategy for designing low-field spintronic functionalities in rare-earth-based antiferromagnets.

As the magnetic field shifts the SSW to lower temperatures, a second-step SSW emerges at 8.9 K under 85 Oe, near the SRT temperature (details for SRT showed in Supplementary Figure 3 and 4). This proximity suggests that the SSWs observed between 90 and 120 Oe may also be multi-step in nature, with the second transition step occurring concurrently with the SRT and thereby becoming obscured. Upon cooling, the Fe^{3+} sublattice undergoes reorientation from the Γ_4 (G_x, F_z) state to the Γ_2 (F_x, G_z) state. $\delta\boldsymbol{m}_{\mathrm{Fe}}$ rotates from the *c*-axis to the *a*-axis between 8.0 K and 6.5 K (as shown in Fig. 3a and Supplementary Figure 4). To investigate the nature of observed SSWs, we define three reference magnetization states: M_1: before the first SSW, M_2: just prior to the onset of the SRT, and M_3: following the completion of the SRT. Fig. 3b compares magnetization changes across these points. When the magnetization difference $\Delta M = M_1 - M_2$, the normalized change $\Delta M/H$ decreases polynomially with increasing field from 50 to 90 Oe, consistent with multi-step SSWs. Beyond 90 Oe, this trend is disrupted, suggesting that part of the SSW is overlapped. However, redefining ΔM as $M_1 - M_3$ recovers the low-field trend. Thus, in YFMO, the SSW expected around 90-120 Oe is not resolved as a distinct step because it overlaps with the SRT process, which gradually rotates $\delta\boldsymbol{m}_{\mathrm{Fe}}$ and smooths the magnetization change.

Differential analysis of the magnetization, shown in Fig. 3c, further supports the presence of concealed multi-step spin switching. The first-step SSW appears as an abrupt change in *dM/dT*, which systematically shifts to lower temperatures under increasing magnetic fields, consistent with the behavior observed in the *M-T* curves. At the SRT region (8.0-6.5 K), a broad peak is observed in d*M*/d*T*, corresponding to the SRT. Superimposed on this broad feature, a sharper anomaly emerges around 8 K in the field range of 90-120 Oe. This anomaly is consistent with a suppressed second-step SSW that becomes obscured in the raw *M-T* data. The inset in Fig. 3c highlights this subtle but reproducible feature near 8 K, indicating that the second-step SSW remains active but embedded within the broader SRT signature. These results confirm that multi-step SSW behavior persists up to 120 Oe, beyond which the system undergoes a pure SRT without SSW features.

Phase evolution and microscopic switching behavior

A schematic illustration of SRT with and without concurrent SSW is shown in Fig. 4. In a conventional SRT, $\delta\mathbf{m}_{\mathrm{Fe}}$ rotates by 90° within the *ac* plane, transitioning from the Γ_4 (G_x, F_z) to the Γ_2 (F_x, G_z) configuration. $\delta\mathbf{m}_R$ simultaneously rotates to maintain its coupling, either parallel or antiparallel, with $\delta\mathbf{m}_{\mathrm{Fe}}$[9,30]. In contrast, when SRT is accompanied by SSW, a subset of R^{3+} moments undergo both a 90° rotation and an additional 180° spin flip (Fig. 4b). This leads to a total angular change of 270° in the *ac* plane and results in a reversal of Fe-*R* coupling from parallel to antiparallel. As a consequence, the total magnetization decreases during the SRT process.

The magnetic field-temperature (*H*-*T*) phase diagram of YFMO is shown in Fig. 5 (constructed from the magnetization data in Figs. 2 and 3, and Supplementary Figure 4). At high temperatures and magnetic fields, the system stabilizes in the Γ_4 (G_x, F_z) magnetic configuration, in which $\mathbf{m}_{\mathrm{Fe}}$ exhibits a small canting along the *c*-axis due to DMI, giving rise to a weak ferromagnetic component $\delta\mathbf{m}_{\mathrm{Fe}}$. Although the R^{3+} sublattice remains paramagnetic above the *R*-ordering temperature T_{N2}, it develops an induced moment $\delta\mathbf{m}_{\mathrm{Yb}}$ via exchange coupling with Fe^{3+}. Neutron diffraction results show that $\delta\mathbf{m}_{\mathrm{Yb}}$ aligns parallel to $\delta\mathbf{m}_{\mathrm{Fe}}$ in the Γ_4 state, as depicted in the yellow region in the phase diagram[8,11,16]. Upon entering the SSW, $\delta\mathbf{m}_{\mathrm{Yb}}$ flips to an antiparallel configuration with respect to $\delta\mathbf{m}_{\mathrm{Fe}}$ (purple region). In the intermediate, multi-step SSW region (blue), partial flipping occurs: Yb^{3+} spins flip antiparallel to Fe^{3+}, while others remain parallel, leading to a mixed magnetic configuration. At lower temperatures, the system undergoes an SRT, where $\mathbf{m}_{\mathrm{Fe}}$ rotates by 90° from the *c*-axis to the *a*-axis, transitioning from the Γ_4 to the Γ_2 state.

$\mathbf{m}_{\mathrm{Yb}}$ also rotate to maintain exchange alignment. In the field range between 90 and 120 Oe, this reorientation is accompanied by an additional spin-flip of Yb^{3+}, establishing a low-temperature state with $\delta\mathbf{m}_{\mathrm{Fe}}$ and $\delta\mathbf{m}_{\mathrm{Yb}}$ aligned antiparallel in the Γ_2 phase.

Theoretical modeling

The coexistence of both conventional and multi-step SSW in YFMO allows for investigating the microscopic origins of SSW in *R*FOs. Within the classical Weiss molecular field framework for antiferromagnetism[31,32], the effective magnetic field $\mathbf{H}_{\mathrm{eff}}$ acting on *R* sublattice is defined as:

$$\mathbf{H}_{\mathrm{eff}} = \mathbf{H} + \mathbf{H}_{\mathrm{M}}, \tag{1}$$

$$\mathbf{H}_{\mathrm{M}} = \mathrm{n}_{(R,\,\mathrm{Fe})}\,\mathbf{M}_{\mathrm{Fe}} + \mathrm{n}_{(R,\,R)}\mathbf{M}_{R}, \tag{2}$$

where $\mathbf{M}_{\mathrm{Fe}}$ and $\mathbf{M}_{R}$ represent the magnetizations of the Fe and *R* sublattices, respectively with negative molecular field coefficients $\mathrm{n}_{(R,\,\mathrm{Fe})}$ and $\mathrm{n}_{(R,\,R)}$, indicating an antiferromagnetic coupling. SSW is thus governed not only by the external magnetic field, but also by the Fe^{3+} molecular field. As temperature decreases, the suppression of thermal fluctuations and enhancement of DMI strengthens $\mathbf{M}_{\mathrm{Fe}}$ and $\mathbf{M}_{R}$, thereby increasing $\mathbf{H}_{\mathrm{M}}$. This temperature- and field-dependent balance of effective field explains the phase evolution in the *H*-*T* diagram (Fig. 5). At high temperatures and strong applied fields, $\mathbf{H}_{\mathrm{eff}}$ is positive and favors a parallel coupling between Fe and Yb spins. In contrast, under lower temperatures and fields, the molecular field dominates and can reverse the sign of $\mathbf{H}_{\mathrm{eff}}$, promoting an antiparallel spin configuration. An SSW would when occur $\mathbf{H}_{\mathrm{eff}}$ crosses zero.

To account for multi-step transitions, we extend the model by partitioning the *R* sublattice into *n* magnetically distinct components, $\{R_i\}$, each experiencing a unique local exchange environment. The effective field on each R_i is:

$$\mathbf{H}_{\mathrm{eff}}^{i}(T) = \mathbf{H} + \sum_{\mathrm{i}=1}^{\mathrm{n}} \mathrm{n}_{(Ri,\,\mathrm{Fe})}\mathbf{M}_{\mathrm{Fe}}(T) + \sum_{j=1}^{\mathrm{n}} \mathrm{n}_{(Ri,\,Rj)}\mathbf{M}_{Rj}(T), \tag{3}$$

where $\mathbf{M}_{\mathrm{Fe}}(T)$ and $\mathbf{M}_{Rj}(T)$ are the temperature-dependent magnetizations, $\mathrm{n}_{(Ri,\,Rj)}$ is the molecular field coefficient between subcomponents R_i and R_j. The spin state of each R_i captures inter-sublattice couplings. The orientation of the R_i spin is governed by the sign of H_{eff}^{i}. H_{eff}^{i} denotes the local projection of the Fe-derived molecular field acting on the different Yb^{3+}. A stepwise type-

II SSW transition occurs when H_{eff}^{i} (T) crosses zero, indicating the inversion of the internal exchange field transmitted from the Fe^{3+} sublattice.

We describe $\mathbf{M}_{\mathrm{Fe}}(T)$ using a phenomenological mean-field expression:

$$\mathbf{M}_{\mathrm{Fe}}(T) = \mathbf{M}_{\mathrm{Fe}}^{0}(1 - T/T_{\mathrm{N}})^{\beta}, \tag{4}$$

where $M_{\mathrm{Fe}}^{0} \approx 4.94\ \mu_{\mathrm{B}}$, $T_{\mathrm{N}} \approx 667.6$ K, and $\beta \approx 0.51$ were extracted from the high-temperature regime (200-300 K) to ensure that the R^{3+} contribution is negligible and also far below the Fe/Mn-sublattice Néel temperature. The R sublattice magnetization is:

$$\mathbf{M}_{R}(T) = \mathbf{M}_{\mathrm{total}}(T) - \mathbf{M}_{\mathrm{Fe}}(T), \tag{5}$$

allowing numerical evaluation of $H_{\mathrm{eff}}^{i}(T)$ and the corresponding critical temperatures T_{SSW}. When the transition temperatures differ among R_i components, sequential SSW naturally emerges. In YFMO, we focus on a two-component model (R_1 and R_2) representing distinct magnetic environments within the R sublattice. The effective field becomes:

$$\mathbf{H}_{\mathrm{eff}}^{i}(T) = \mathbf{H} - 4.94(\mathrm{n}_{(\mathrm{R1,\,Fe})} + \mathrm{n}_{(\mathrm{R2,\,Fe})})(1\text{-}T/667.6)^{0.51} - \mathrm{n}_{(R1,\,R2)}\mathbf{M}_{R}^{\mathrm{interp}}(T), \tag{6}$$

where $\mathbf{M}_{R}^{\mathrm{interp}}(T)$ is interpolated from experimental data. The model reproduces the observed single- and multi-step SSW transitions with high fidelity.

A schematic energy diagram (Fig. 6) illustrates the microscopic mechanisms. At high temperatures, both R_1 and R_2 remain aligned due to weak molecular fields. Upon cooling, $\mathbf{H}_{\mathrm{eff}}^{1}$ first crosses zero at T_{SSW1}, inducing the first SSW event (SSW1). At a lower temperature T_{SSW2}, $\mathbf{H}_{\mathrm{eff}}^{2}$ also changes sign, completing the multi-step SSW. At elevated fields, the simultaneous vanishing of $\mathbf{H}_{\mathrm{eff}}^{1}$ and $\mathbf{H}_{\mathrm{eff}}^{2}$ merges the two transitions into a single SSW. In the intermediate field range (50-90 Oe), the competition between applied and molecular fields again separates the transitions, giving rise to reentrant multi-step SSW behavior. This unified, energy-based framework captures both conventional single-step and multi-step SSW processes, offering a predictive description of spin-state transitions in an insulating orthoferrite through subtle modulation of the internal field by Mn substitution. Unlike current-driven switching in metallic systems, SSW provides a clean platform to explore intrinsic-field-governed spin reversal dynamics.

The extended Weiss model established here captures the key features of multi-step SSW and can serve as a general basis for analyzing multi-level spin transitions and guiding the design of programmable antiferromagnetic spintronic systems.

Conclusions

In conclusion, we have reported the observation of both conventional SSW and multi-step SSW in a transition-metal-doped *R*FO single crystal, YFMO. Mn doping effectively weakens the molecular field from the Fe^{3+} sublattice, enabling controlled spin flipping of Yb^{3+} moments and revealing type-II and multi-step SSW behaviors. To interpret these transitions, we introduced an effective field that incorporates both internal molecular and external magnetic fields, extending the classical Weiss model for antiferromagnetism. This model provides a quantitative basis for understanding the onset and progression of SSW transitions. Our results show that YFMO can access low-energy spin configurations through either single-step or sequential spin reversals, in which the rare-earth sublattice couples antiparallel to the Fe sublattice. The field-tunability of multi-step SSW further suggests the feasibility of programmable spin states and polymorphic memory functionalities. These findings establish a platform for controlling spin states in orthoferrites through internal field engineering and open avenues for rare-earth-based spintronic devices.

Methods

Single crystal growth

A single crystal of YFMO was grown by optical floating zone method (FZ-T-10000-H-VI-P-SH, Crystal Systems Corp.). The feed and seed rods were prepared via conventional solid-state reaction and counter-rotated at 30 rpm to ensure uniform compositional mixing. The molten zone was translated at a rate of 3.0 mm h^{-1} in ambient air with an airflow of 1.5 L min^{-1}. All growth procedures were performed in air without additional gas flow control. The measured sample size was $a \times b \times c = 2.75 \times 2.81 \times 2.02$ mm^3, and the demagnetization factor was estimated as N $\approx$ 0.4.

Structural measurements

Crystal orientation was confirmed using an X-ray Laue back-reflection diffraction (Try-SE. Co, Ltd., Co Kα source). Both surface and powder XRD measurements were conducted on a Bruker D2 DISCOVER diffractometer with a Cu Kα target (λ = 1.54178 Å). XPS experiments were performed using a monochromatic Al Kα source (hν = 1486.6 eV) and a PHOIBOS 150 hemispherical analyzer (SPECS Surface Nano Analysis GmbH) equipped with a 2D CMOS detector. All XPS experiments were conducted in an ultrahigh vacuum (UHV) system (base pressure $< 1 \times 10^{-10}$ mbar) and following in situ annealing at 600 °C to remove surface contamination. The XPS spectra were calibrated using the C 1*s* peak at 284.6 eV.

Magnetic measurements

Magnetic measurements were carried out utilizing a vibrating sample magnetometer (VSM) module integrated into a Physical Property Measurement System (PPMS-14T, Quantum Design). The magnet was demagnetized before each measurement using the standard Magnet Reset routine to ensure a residual field below 1 Oe. The applied magnetic field was along the crystallographic *a*-, *b*-, or *c*-axis, as specified for each measurement. The field uniformity of the PPMS-14T magnet is approximately ±0.1% over a 5.5 cm sample space in the 14 T mode, with a field resolution better than 0.1 Oe. The temperature range for measurements was 2.0-300.0 K, with temperature stability better than 0.2% below 10 K and 0.02% above 10 K. The field sweep (charging) rate was set to 25 Oe s^{-1}, and the temperature sweep rate to 2 K min^{-1}, ensuring high precision and reproducibility in both *M*-*H* and *M*-*T* measurements.

Data availability

The supplementary data underlying all main figures and supplementary figures in this study have been deposited in the Figshare repository under the permanent identifier 10.6084/m9.figshare.30938477. All the data supporting the findings of this study are available from the corresponding author (email: sxcao@shu.edu.cn) upon request.

References

1. Lebrun, R. *et al.* Tunable long-distance spin transport in a crystalline antiferromagnetic iron oxide. *Nature* **561**, 222–225 (2018).
2. Baierl, S. *et al.* Terahertz-driven nonlinear spin response of antiferromagnetic nickel oxide. *Phys. Rev. Lett.* **117**, 197201 (2016).
3. Jia, F. *et al.* Understanding the intrinsic piezoelectric anisotropy of tetragonal ABO_3 perovskites through a high-throughput study. *npj Comput Mater* **11**, 6 (2025).
4. Schlauderer, S. *et al.* Temporal and spectral fingerprints of ultrafast all-coherent spin switching. *Nature* **569**, 383–387 (2019).
5. Li, X. *et al.* Observation of Dicke cooperativity in magnetic interactions. *Science* **361**, 794–797 (2018).
6. Das, S. *et al.* Anisotropic long-range spin transport in canted antiferromagnetic orthoferrite $YFeO_3$. *Nat Commun* **13**, 6140 (2022).
7. Becker, S. *et al.* Electrical detection of the spin reorientation transition in antiferromagnetic $TmFeO_3$ thin films by spin Hall magnetoresistance. *Phys. Rev. B* **103**, 024423 (2021).
8. Nikitin, S. E. *et al.* Decoupled spin dynamics in the rare-earth orthoferrite $YbFeO_3$: Evolution of magnetic excitations through the spin-reorientation transition. *Phys. Rev. B* **98**, 064424 (2018).
9. Zhao, W. Y. *et al.* Spin reorientation transition in dysprosium-samarium orthoferrite single crystals. *Phys. Rev. B* **91**, 104425 (2015).
10. Fita, I. *et al.* Common exchange-biased spin switching mechanism in orthoferrites. *Phys. Rev. B* **98**, 094421 (2018).
11. Li, E. Y. *et al.* Spin switching in single crystal $PrFeO_3$ and spin configuration diagram of rare earth orthoferrites. *Journal of Alloys and Compounds* **811**, 152043 (2019).
12. Zhao, G. *et al.* 4*f*-3*d* interaction dominated field tailoring spin switching in rare earth doped $Dy_{0.5}Er_{0.5}FeO_3$ single crystal. *Applied Materials Today* **23**, 101070 (2021).
13. Yang, W. *et al.* Multiple spin switching and magnetocaloric effects in orthoferrite $Yb_{0.25}Tb_{0.75}FeO_3$ single crystal. *Journal of Alloys and Compounds* **962**, 171055 (2023).
14. Zhang, J. *et al.* Spin reorientation and rare earth antiferromagnetic transition in single crystal $Sm_{0.15}Dy_{0.85}FeO_3$. *Journal of Alloys and Compounds* **804**, 396–400 (2019).
15. Wu, H. *et al.* Twofold spin reorientation and field-induced incomplete phase transition in single-crystal $Dy_{0.5}Pr_{0.5}FeO_3$. *Phys. Rev. B* **90**, 144415 (2014).
16. White, R. L. Review of recent work on the magnetic and spectroscopic properties of the rare-earth orthoferrites. *J. Appl. Phys.* **40**, 1061–1069 (1969).
17. Fan, W. *et al.* Thermal control magnetic switching dominated by spin reorientation transition in Mn-doped $PrFeO_3$ single crystals. *Front. Phys.* **17**, 33504 (2022).
18. Yang, W. *et al.* Room-temperature spin reorientation transition and low-temperature significant magnetothermal effect in Mn-doped $DyFeO_3$ single crystals. *Ceram. Int.* **50**, 12279–12286 (2024).
19. Kumar, A. *et al.* Origin of natural and magnetic field induced polar order in orthorhombic $PrFe_{1/2}Cr_{1/2}O_3$. *Phys. Rev. B* **104**, 035101 (2021).
20. Nakhaei, M., Bremholm, M. & Khoshnoud, D. S. Structural and Magnetic Properties of RMO_3 (R = Pr, Nd and M = Fe, Co) Perovskites. *J Supercond Nov Magn* **34**, 3255–3266 (2021).

21. Bhat, M. A., Rana, P., Mir, F. A. & Pathak, D. “A brief study on exploration of Ni doped $PrFeO_3$ perovskite as multifunctional material”. *J Mater Sci: Mater Electron* **34**, 269 (2023).
22. Rietveld, H. M. A profile refinement method for nuclear and magnetic structures. *J Appl Crystallogr* **2**, 65–71 (1969).
23. Ma, X. *et al.* Field tunable spin switching in perovskite $YbFeO_3$ single crystal. *Mater. Today Commun.* **27**, 102438 (2021).
24. Nagata, Y. *et al.* Magnetic properties of $RFe_{1-x}Mn_xO_3$ (R = Pr, Gd, Dy). *J. Magn. Magn. Mater.* **237**, 250–260 (2001).
25. Deka, B., Ravi, S., Perumal, A. & Pamu, D. Effect of Mn doping on magnetic and dielectric properties of $YFeO_3$. *Ceramics International* **43**, 1323–1334 (2017).
26. Yang, W. *et al.* Source data for observation and extended Weiss modelling of multi-step type-II spin switching in Mn doped $YbFeO_3$. 1223444 Bytes figshare https://doi.org/10.6084/M9.FIGSHARE.30938477 (2025).
27. Momma, K. & Izumi, F. *VESTA 3* for three-dimensional visualization of crystal, volumetric and morphology data. *J Appl Crystallogr* **44**, 1272–1276 (2011).
28. Anderson, P. W. Antiferromagnetism. Theory of superexchange interaction. *Phys. Rev.* **79**, 350–356 (1950).
29. Bazaliy, Ya. B., Tsymbal, L. T., Kakazei, G. N., Kamenev, V. I. & Wigen, P. E. Measurements of spin reorientation in $YbFeO_3$ and comparison with modified mean-field theory. *Phys. Rev. B* **72**, 174403 (2005).
30. Skorobogatov, S. A. *et al.* Pressure control of the spin reorientation transition in the rare-earth orthoferrite $YbFeO_3$. *Phys. Rev. B* **108**, 054432 (2023).
31. Smart, J. S. Molecular field treatment of ferromagnetism and antiferromagnetism. *Phys. Rev.* **86**, 968–974 (1952).
32. Li, Y.-Y. Application of the Bethe-Weiss method to the theory of antiferromagnetism. *Phys. Rev.* **84**, 721–730 (1951).

Acknowledgments

This work was supported by the National Natural Science Foundation of China [Grant numbers 12374116]. X.M. was supported by the fellowship from the China Postdoctoral Science Foundation [Certificate Number: 2024M751931]. Y.D. was supported by the project Centre for Advanced Laser Techniques (CALT), co-funded by the European Union through the European Regional Development Fund under the Competitiveness and Cohesion Operational Programme [Grant No. KK.01.1.1.05.0001].

Author contribution

W.Y. conceived the project, conducted the experiments and the theoretical model, analyzed the data, and wrote the initial draft. H.P. contributed to magnetic measurements. Y.G. carried out the

X-ray photoelectron spectroscopy experiments with Y.D.'s supervision. X.M., R.J., B.K., and J.G. assisted with data analysis and manuscript revision. S.C. provided overall supervision, contributed to data analysis, and revised the manuscript.

All authors discussed the results and approved the final version of the manuscript.

Competing interests

The authors declare no competing interests.

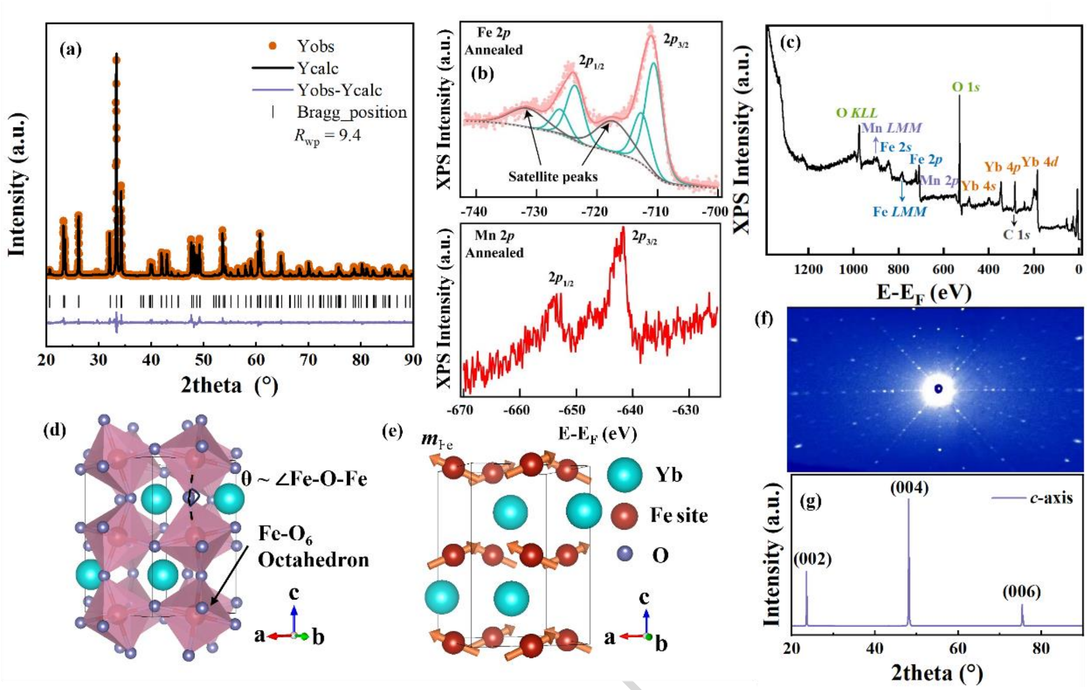

Fig. 1| Structural and chemical characterization of YbFe$_{0.95}$Mn$_{0.05}$O$_3$ single crystal. (**a**) Rietveld refinement of the powder X-ray diffraction spectrum using FullProf Suite, based on the *Pbnm* orthorhombic perovskite structure and reference PDF file PDF #47-0070 (R_{wp} = 9.4, χ^2 = 1.2). (**b**) High-resolution X-ray photoelectron spectra of Fe 2*p* and Mn 2*p* collected after annealing at 600 °C for 30 min, showing characteristic spin-orbit splitting. (**c**) Survey X-ray photoelectron spectra after annealing. The spectra were charge-corrected using the C 1*s* peak at 284.6 eV. (**d**) Crystal structure model with Fe-O-Fe bond angle of 141.35°, drawn using VESTA[20]. Green, red, and purple spheres represent Yb, Fe/Mn, and O atoms, respectively. (**e**) Magnetic structure of the Fe sublattice showing the Γ_4 (G_x, F_z) canted antiferromagnetic configuration, with arrows indicating the Fe^{3+} magnetic moments. (**f**) Laue back-reflection X-ray pattern, confirming high crystal orientation. (**g**) High-resolution X-ray diffraction pattern along the *c*-axis, displaying (00*l*) reflections without detectable impurity peaks.

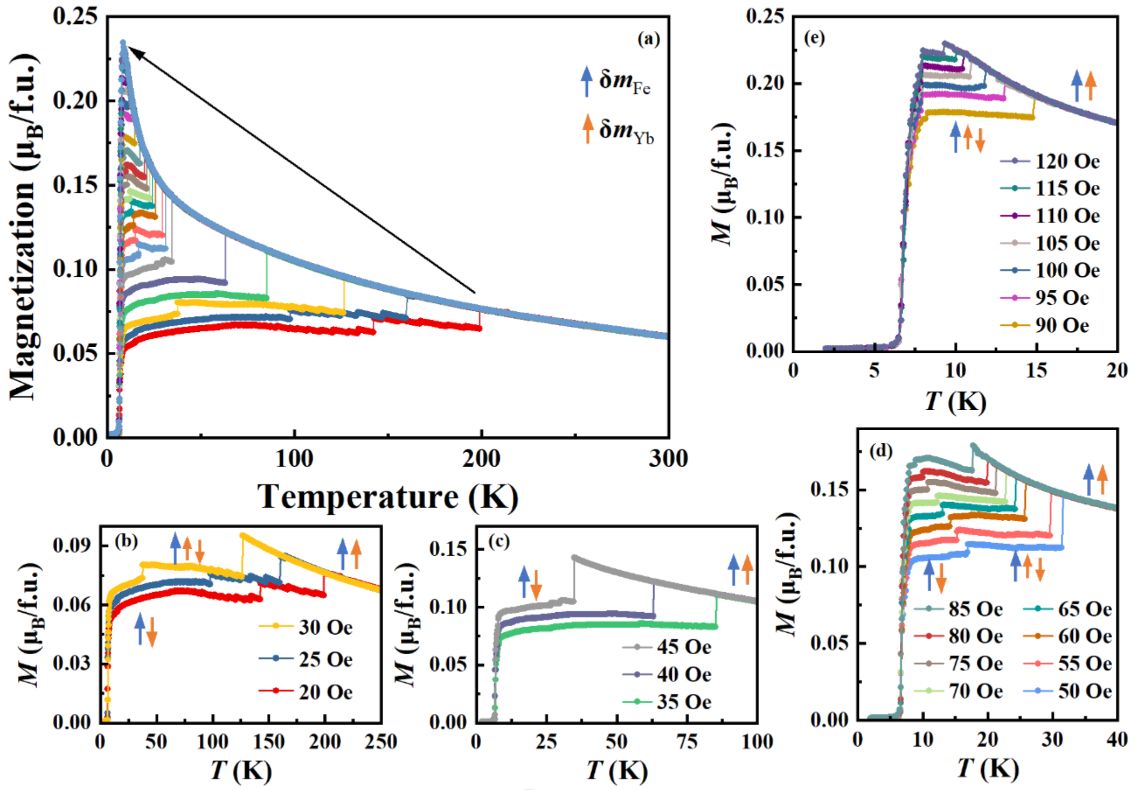

Fig. 2| Field-tunable spin switching. Temperature dependence of the magnetization curves measured along the *c*-axis under various magnetic fields. (**a**) Overview of field-cooled cooling curves under 20-125 Oe, showing the evolution of spin switching. (**b-e**) Representative temperature dependence of the magnetization curves highlighting the transition from multi-step to single-step spin switching regimes as the applied field increases. The blue and orange arrows represent the net magnetic moments of Fe^{3+} and Yb^{3+}, respectively.

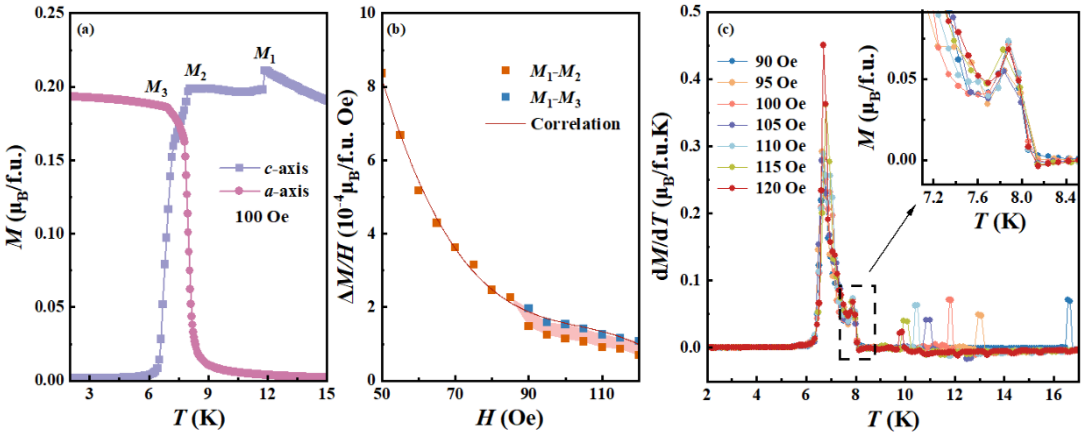

Fig. 3| Coupling between spin switching and spin reorientation transition. (**a**) Magnetization versus temperature curves along the *a*- and *c*-axes in field-cooled-cooling mode under 100 Oe, data for other magnetic fields in Supplementary Figure 2. (**b**) Field dependence of the normalized magnetization changes Δ*M*/*H*, where Δ*M* is defined as the difference between magnetization at states labelled M_1, M_2, and M_3 in panels (a), Fig. 2e and Supplementary Figure 4. (**c**). Temperature derivative of magnetization under 90-120 Oe, with the inset highlighting the second-step spin switching peak near the spin reorientation transition region.

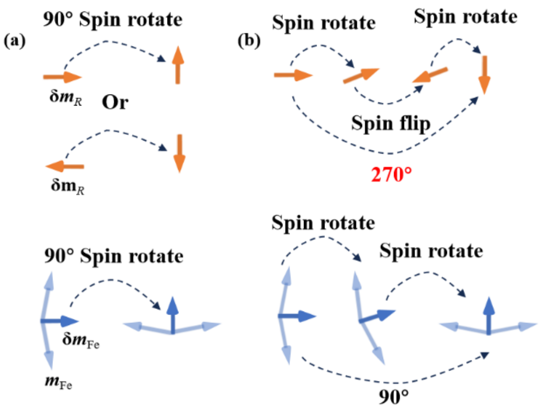

Fig. 4 | Spin dynamic process of spin reorientation transition. (**a**) Conventional spin reorientation with 90° rotation of Fe^{3+} spin (blue arrow) and R^{3+} spins (orange arrow). (**b**) Spin reorientation coupled with spin switching, where a subset of R^{3+} moments flips by 180° after rotation. Blue and orange arrows denote Fe^{3+} and R^{3+} spins; light blue arrows represent Fe^{3+} spins.

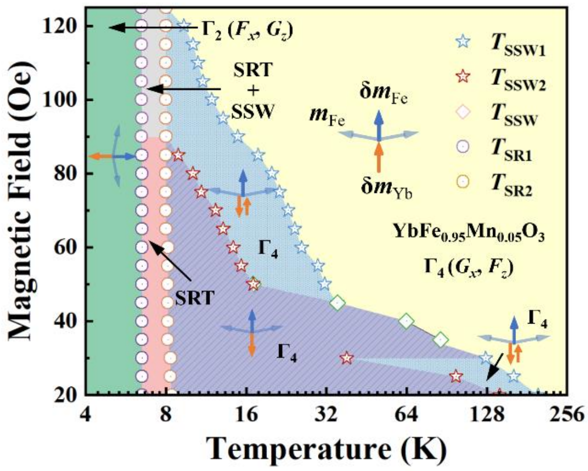

Fig. 5 | Magnetic field-temperature phase diagram. Colored regions represent distinct magnetic phases, defined by the configuration of the Fe^{3+} and Yb^{3+} sublattices. Blue and orange arrows show net magnetic moments of Fe^{3+} and Yb^{3+} sublattices, respectively; light blue arrows indicate Fe^{3+} spins.

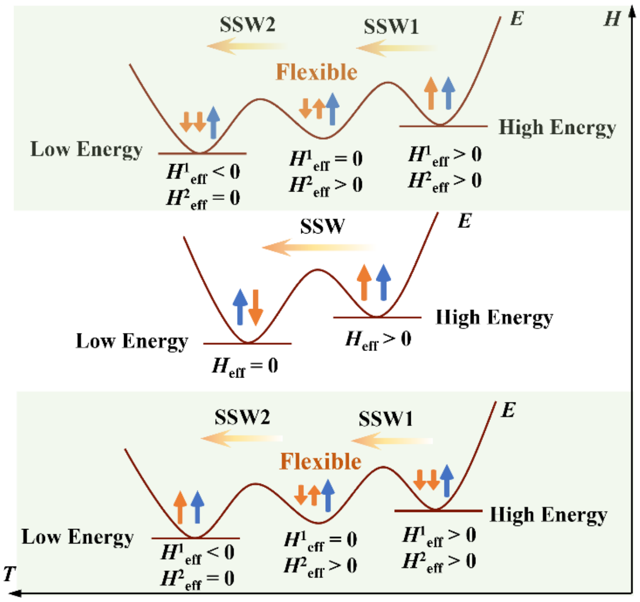

Fig. 6 | Illustration of field-modulated single and multi-step spin switching. Temperature-driven sequential switching of two inequivalent R^{3+} sublattices (R_1 and R_2) under modulated effective field. Orange arrows represent R^{3+} net magnetic moments in distinct local environments and blue arrows represent Fe^{3+} net magnetic moments.

Editor Summary-

Due to the strong exchange interactions between the rare-earth and iron sublattices, rare-earth orthoferrites, such as $YbFeO_3$, offer a rich platform for exploring spin dynamics and spin transport phenomena. Here, the authors report multi-step type-II spin switching in Mn-doped $YbFeO_3$ and investigate the underlying mechanism using an extended Weiss model.

Peer Review Information-

Communications Physics thanks Krishnamurthy Jyothinagaram and the other, anonymous, reviewer(s) for their contribution to the peer review of this work. A peer review file is available.

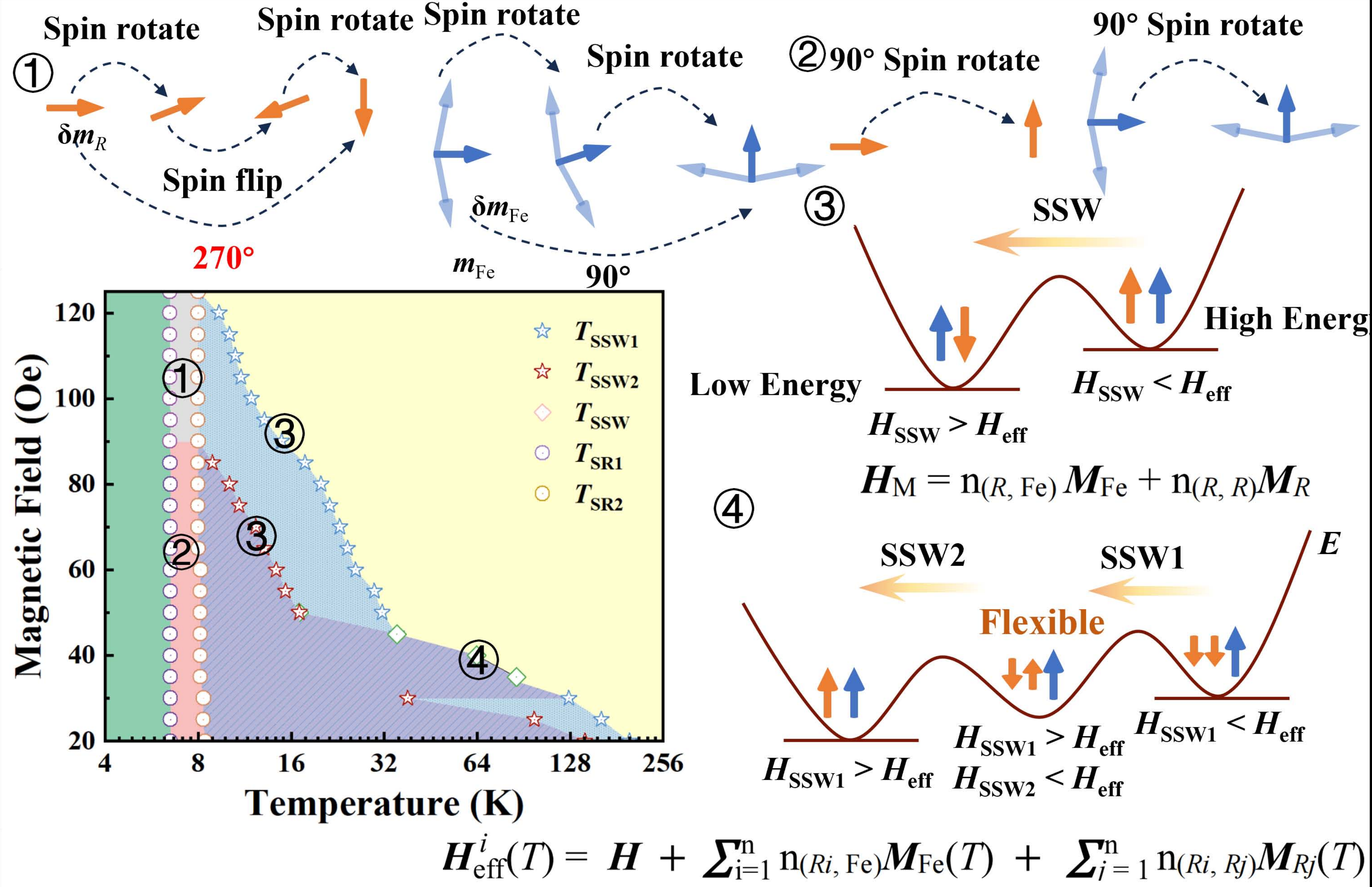
①
Spin rotate
Spin rotate
Spin flip
δm_R
270°
Spin rotate
Spin rotate
δm_{Fe}
m_{Fe}
90°
② 90° Spin rotate
90° Spin rotate
③
SSW
High Energ
Low Energy
$H_{SSW} > H_{eff}$
$H_{SSW} < H_{eff}$
$H_M = n_{(R,\,Fe)} M_{Fe} + n_{(R,\,R)} M_R$
④
SSW2
SSW1
E
Flexible
$H_{SSW1} > H_{eff}$
$H_{SSW1} > H_{eff}$
$H_{SSW2} < H_{eff}$
$H_{SSW1} < H_{eff}$
Magnetic Field (Oe)
120
100
80
60
40
20
Temperature (K)
4
8
16
32
64
128
256
T_{SSW1}
T_{SSW2}
T_{SSW}
T_{SR1}
T_{SR2}
①
②
③
③
④
$H^i_{eff}(T) = H + \sum_{i=1}^{n} n_{(Ri,\,Fe)} M_{Fe}(T) + \sum_{j=1}^{n} n_{(Ri,\,Rj)} M_{Rj}(T)$